Soft Matter

PAPER

Cite this: *Soft Matter*, 2019, **15**, 2627

Active chiral particles under confinement: surface currents and bulk accumulation phenomena

Lorenzo Caprini[a] and Umberto Marini Bettolo Marconi *[bc]

Received 10th December 2018,
Accepted 14th February 2019

DOI: 10.1039/c8sm02492h

rsc.li/soft-matter-journal

In this work, we study the stationary behavior of an assembly of independent chiral active particles under confinement by employing an extension of the active Ornstein–Uhlenbeck model. The chirality modeled by means of an effective torque term leads to a drastic reduction in the accumulation near the walls with respect to the case without handedness and to the appearance of currents parallel to the container walls accompanied by a large accumulation of particles in the inner region. In the case of two-dimensional chiral particles confined by harmonic walls, we determine the analytic form of the distribution of positions and velocities in two different situations: a rotationally invariant confining potential and an infinite channel with parabolic walls. Both these models display currents and chirality induced inner accumulation. These phenomena are further investigated by means of a more realistic description of a channel, where the wall and bulk regions are clearly separated. The corresponding current and density profiles are obtained by numerical simulations. At variance with the harmonic models, the third model shows a progressive emptying of the wall regions and the simultaneous enhancement of the bulk population. We explain such a phenomenon in terms of the combined effect of wall repulsive forces and chiral motion and provide a semiquantitative description of the current profile in terms of effective viscosity of the chiral gas.

1 Introduction

The dynamics of self-propelled particles is an exciting new area of research at the frontier between physics, biology and bio-engineering.[1–4] These particles are ubiquitous in nature or can be artificially created and employed in the near future in tasks such as targeted drug delivery and nanosurgery. Examples of the first category are bacteria, ciliates, *Synechococcus* a type of blue-green alga, and sperm cells, while artificial self-propellers are represented by Janus particles catalytically driven or magnetic microparticles subject to a magnetic field. Each particle, whose size may range from 10 μm up to several microns, consumes energy from the environment in order to move and is fueled either by metabolic processes or by chemical reactions: *E. coli* move forward through rotational motion of their spiral-shaped flagella while synthetic Janus colloids are driven by a catalytic chemical reaction on their surface.

A small departure from the right-left symmetry relative to the propulsion axis of the self-propelled particles or an external magnetic field is sufficient to determine circle swimming in two dimensions or helical swimming in three dimensions, a phenomenon termed chirality or handedness. Indeed, in nature one observes spiral-like swimming trajectories in *E. coli* bacteria[5,6] and spermatozoa in bulk suspensions[7] or circle-like motion near a planar substrate[8] and clockwise treadmilling in FtsZ proteins on membranes.[9]

Analogous chiral trajectories are produced by artificial microswimmers, for instance, L-shaped particles.[10,11] In nature, magnetotactic bacteria are widespread motile prokaryotes, having an organelle called magnetosome which causes the cell to behave like a miniature compass and swim parallel to the magnetic field lines.[12,13] The direction of the magnetic field is so crucial that this kind of bacterium dies when taken to the opposite hemisphere of Earth.

As discussed by Ten Hagen *et al.*[14] a system of self-propelled particles can be described at two different levels: (i) a fine-grained level fully taking into account the self-propulsion mechanism, the degrees of freedom of microswimmers, such as moving internal elements, and the solvent hydrodynamics,[15] (ii) a coarse-grained level where the motion of microswimmers is modeled by using the Brownian overdamped equations and the self-propulsion is represented in terms of effective forces and torques.[16] In the following, it was convenient for us, following the literature in the field, to adopt the second level of description which allows a straightforward application of the tools of statistical mechanics and computer simulation for large collections of active particles. Among these tools there

[a] *Gran Sasso Science Institute (GSSI), Via. F. Crispi 7, 67100 L'Aquila, Italy*
[b] *School of Sciences and Technologies, Università di Camerino, via Madonna delle Carceri, 62032, Camerino, Italy. E-mail: umberto.marinibettolo@unicam.it*
[c] *INFN, Perrugia, Italy*

are two popular theoretical approaches for the study of active particles: the active Brownian particle (ABP) model,[17,18] and the active Ornstein–Uhlenbeck particle (AOUP) model.[19] Both models represent the microswimmer motion through a viscous solvent by means of Langevin overdamped dynamics and include the distinguishing feature of active particles, namely the self-propulsion mechanism as an effective force term. Such a self-propulsion force has the following properties: (a) it is typically noisy and its orientation is random, (b) active forces acting on different self-propelled particles are mutually independent and (c) the direction of driving persists over time scales of the order of the microseconds. As briefly discussed in the next Section, the ABP and the AOUP differ by the way the self-propulsion force is modeled, but in spite of that many important aspects of their nonequilibrium behavior are similar. So far, the mechanism responsible for the active chiral behavior has been included only in the ABP by adding an effective constant torque term in the corresponding Langevin equation.[16] Chirality could also be induced by the non spherical shape of the particles, but this mechanism is not treated in the present work. Such a torque induces a systematic drift in the orientation of active particles, *i.e.* a rotation with a constant angular speed of the active velocity, leading to helical trajectories in three dimensions and to circular ones in two dimensions.

While the effect of chirality on the bulk behavior of self-propelled particles has been investigated,[11] the properties of the self-propelled chiral particles under confinement are not so well known and understood. Confining surfaces may induce surface accumulation, sliding motion and selection of active particles according to their chirality[20–22] and therefore it is interesting to investigate under which conditions these effects can be enhanced or suppressed.

In the present work, we focus on the properties of confined chiral particles and motivated by the simpler mathematical structure of the AOUP, which facilitates theoretical treatments, we extend these to account for chiral effects. As in the case of the ABP, this goal is achieved by adding a torque term to the self-propulsion.

The paper is organized as follows: in Section 2 we introduce the chiral active Ornstein–Uhlenbeck particle (CAOUP) model, in Section 3 we study the special case of the CAOUP confined in a two-dimensional harmonic trap, and in Section 4 we study the behaviour of the model in the case of confinement in a parabolic channel and in a slit. Finally, in Section 5 we present the conclusions and discuss some future directions.

2 Planar chiral active motion

In the following, we describe the assembly of N mutually independent active chiral particles moving in the two dimensional (x, y) plane. Each particle at position $\mathbf{x}_i$ is subject to four kinds of driving forces: an active or self-propulsion force, $\mathbf{f}_i^a$, a drag force, $-\gamma\dot{\mathbf{x}}_i$ due to the friction with the solvent, a white noise force $\gamma\sqrt{2D_\mathrm{t}}\boldsymbol{\xi}_i$ representing the thermal agitation of the solvent, whose intensity depends on the thermal diffusion coefficient, D_t, and a force, $-\nabla\phi(\mathbf{x}_i)$ due to a potential, ϕ which confines their motion in a restricted region of the two-dimensional space. The active force, $\mathbf{f}_i^a = \gamma v_0\mathbf{e}_i$ has a constant magnitude proportional to a velocity v_0 and a direction $\mathbf{e}_i \equiv (\cos\theta_i, \sin\theta_i)$ dependent on an angle $\theta_i(t)$ undergoing unbiased rotational diffusion with rotational diffusion coefficient D_r. Inertial effects are neglected because of the low Reynolds number regime as well as the hydrodynamic effects and the solvent reaction. van Teeffelen *et al.*[16] have extended the standard ABP model to account for the chiral motion of microswimmers by adding a new ingredient: they imposed a constant angular drift of amplitude Ω to the dynamics of the angle $\theta_i(t)$ to represent an effective constant torque uniformly applied to the particles. The resulting chiral ABP model is described by the following stochastic equations:

$$\gamma\dot{\mathbf{x}}_i = -\nabla\phi(\mathbf{x}_i) + \gamma\sqrt{2D_\mathrm{t}}\boldsymbol{\xi}_i + \mathbf{f}_i^a, \tag{1}$$

$$\dot{\mathbf{e}}_i = \left(\sqrt{2D_\mathrm{r}}w_i + \Omega\right)\hat{\mathbf{z}}\times\mathbf{e}_i, \tag{2}$$

where $\hat{\mathbf{z}}$ is the unit vector normal to such a plane, $\boldsymbol{\xi}_i$ and w_i are independent Gaussian noises with δ-correlated components, unit variance and zero mean. The torque turns the standard exponential form of the autocorrelation function of the orientation vector into a damped oscillatory behavior

$$\langle\mathbf{e}_i(t)\cdot\mathbf{e}_j(0)\rangle = \delta_{ij}\mathrm{e}^{-D_\mathrm{r}t}\cos(\Omega t), \tag{3}$$

where $t > 0$. Notice that when $|\Omega t| > \pi/2$ the force autocorrelation function becomes negative.

A series of interesting studies of the chiral ABP have been conducted by various authors,[20,22–24] and they mainly rely on numerical simulations and/or the analysis of the low noise, quasi-deterministic behavior of eqn (1) and (2).

Hereafter, motivated by the success of the active Ornstein–Uhlenbeck model in reproducing and predicting the main behaviors of non-chiral microswimmers,[25–27] we consider its chiral extension. Moreover, the AOUP is considered to be a valid alternative tool to investigate the properties of active particles because of the feature which makes it analytically more treatable than the ABP, namely the property that the fluctuations of the self-propulsion force are Gaussian. We introduce the chiral version of the AOUP model by assuming the same governing eqn (1) for $\mathbf{x}_i$ as in the ABP, but writing the dynamics of the active force $\mathbf{f}_i^a = \gamma\boldsymbol{u}_i$ as:

$$\dot{\mathbf{u}}_i = -\frac{\mathbf{u}_i}{\tau} + \Omega\hat{\mathbf{z}}\times\mathbf{u}_i + \frac{\sqrt{2D_\mathrm{a}}}{\tau}\boldsymbol{\eta}_i, \tag{4}$$

where $\boldsymbol{\eta}_i$ is the Gaussian noise and each component of $\mathbf{u}_i$ evolves according to the Ornstein–Uhlenbeck process of characteristic time, τ and strength D_a and is subject to a tangential drift at a fixed frequency Ω around an axis orthogonal to the plane of motion. It is very simple to show that, in the case of freely moving particles ($\phi = 0$), the two-time correlation functions of the chiral versions of the ABP and the AOUP

are similar. A brief calculation gives the following two-time average:

$$\langle u_\alpha(t)u_\alpha(0)\rangle = \frac{D_a}{\tau}e^{-\frac{t}{\tau}}\cos(\Omega t), \tag{5}$$

where Greek indices denote Cartesian components and the particle index will be omitted from now on. Although it is known that even in the non-chiral case there are some important differences between the two models (*e.g.* the stationary distribution of f_α^a is circular in the ABP and Gaussian in the AOUP), previous studies[28,29] have shown that they share many important aspects of their nonequilibrium behavior. It is not too unlikely to assume that this holds true even in the case of angular drift. Thus, neglecting the autocorrelation functions of the self-propulsion $\mathbf{f}_i^a(t)$ beyond the second order and noticing that eqn (3) and (5) have the same functional form, we establish the following mapping between the parameters of the two models by making the correspondence:

$$v_0^2 = \frac{D_a}{\tau}d, \tag{6}$$

where d is the dimensionality.

For theoretical work it is convenient to transform eqn (1) and (4) into a system of equations involving the effective velocity, $\mathbf{v}$ defined as $\mathbf{v} = \mathbf{u} - \frac{\nabla\phi}{\gamma}$ and generalizing the transformation of ref. 30 and 31 we obtain a new set of equations (see Appendix A6):

$$\dot{\mathbf{x}} = \mathbf{v} + \sqrt{2D_t}\boldsymbol{\xi}, \tag{7}$$

$$\begin{aligned}\dot{\mathbf{v}} &= -\frac{1}{\tau}\left(\frac{1}{\gamma}\nabla\phi + \boldsymbol{\Gamma}(\mathbf{x})\cdot\mathbf{v}\right) + \Omega\hat{\mathbf{z}}\times\left(\mathbf{v}+\frac{1}{\gamma}\nabla\phi\right)\\ &\quad + \frac{\sqrt{2D_a}}{\tau}\boldsymbol{\eta} + \frac{\mathbf{I}-\boldsymbol{\Gamma}(\mathbf{x})}{\tau}\sqrt{2D_t}\boldsymbol{\xi},\end{aligned} \tag{8}$$

where $\mathbf{I}$ is the identity matrix and $\boldsymbol{\Gamma}$ is an effective friction tensor given by:

$$\Gamma_{\alpha\beta}(\mathbf{x}) = \delta_{\alpha\beta} + \frac{\tau}{\gamma}\nabla_\alpha\nabla_\beta\phi(\mathbf{x}). \tag{9}$$

Such a transformation maps the original problem of an active particle onto the dynamics of a fictitious passive particle, immersed in a heat bath of amplitude $\sqrt{2D_a}/\tau$. The fictitious particle experiences: (i) a deterministic force proportional to the potential gradient (the first term in the r.h.s. of eqn (8)), (ii) a Stokes force dependent on the second derivative of the potential (the second term in the r.h.s.), (iii) an effective Lorentz force proportional to the torque Ω and orthogonal to the velocity $\mathbf{v}$ and (iv) a term proportional to Ω and orthogonal to the potential gradient. Hereafter, the thermal diffusion coefficient, D_t is set equal to zero, not only for simplifying the analytical work but also because it is often much smaller than D_a.[32] For the following analysis, it is convenient to write the Fokker–Planck equation (FPE)[33] for the $P(\mathbf{x}, \mathbf{v}, t)$ distribution corresponding to the dynamics (7) and (8). In the limit of vanishing thermal noise we write:

$$\begin{aligned}\frac{\partial P(\mathbf{x},\mathbf{v},t)}{\partial t} &= \frac{D_a}{\tau^2}\sum_\alpha\frac{\partial^2 P(\mathbf{x},\mathbf{v},t)}{\partial v_\alpha^2} - \sum_\alpha v_\alpha\frac{\partial P(\mathbf{x},\mathbf{v},t)}{\partial x_\alpha}\\ &\quad + \sum_\alpha\frac{\partial}{\partial v_\alpha}\frac{1}{\tau}\left(\sum_\beta\left(\delta_{\alpha\beta}+\frac{\tau}{\gamma}\phi_{\alpha\beta}-\Omega\tau\varepsilon_{\alpha\beta}\right)v_\beta P(\mathbf{x},\mathbf{v},t)\right)\\ &\quad + \sum_\alpha\frac{\partial}{\partial v_\alpha}\frac{1}{\tau}\left(\sum_\beta\left(\delta_{\alpha\beta}-\Omega\tau\varepsilon_{\alpha\beta}\right)\frac{\phi_\beta}{\gamma}P(\mathbf{x},\mathbf{v},t)\right),\end{aligned} \tag{10}$$

where for notational convenience we adopted an explicit Cartesian representation, using Greek indices to denote two dimensional vector components, introduced the symbols ϕ_α and $\phi_{\alpha\beta}$ for the first and second partial derivatives of the potential, respectively, and the symbol $\varepsilon_{\alpha\beta}$ for the antisymmetric 2×2 tensor such that $\varepsilon_{yx} = -\varepsilon_{xy} = 1$.

2.1 Detailed balance

At variance with the standard AOUP model ($\Omega = 0$) in order to obtain the steady state solution of the FPE (10) we ought to solve the second order partial differential equation corresponding to the vanishing of the phase-space divergence of the probability current[34] $\mathbf{I}_\alpha = ((I_\alpha)_\mathbf{x}, (I_\alpha)_\mathbf{v})$, where $\alpha = x, y$:

$$\mathbf{div}_\alpha\cdot\mathbf{I}_\alpha = \sum_\alpha\frac{\partial}{\partial x_\alpha}(I_\alpha)_\mathbf{x} + \frac{\partial}{\partial v_\alpha}(I_\alpha)_\mathbf{v}. \tag{11}$$

It is convenient to split the probability current into a reversible and an irreversible contribution, *i.e.* $\mathbf{I}_\alpha = \mathbf{I}_\alpha^{rev} + \mathbf{I}_\alpha^{irr}$, according to the their parity under time reversal, *i.e.* the components $(\mathbf{x}, \mathbf{v})$ of the reversible (irreversible) part of the current are transformed under time-reversal in the same (opposite) way as the time derivative of $(\mathbf{x}, \mathbf{v})$, respectively. Explicitly, the components of the probability current are:

$$(I_\alpha^{rev})_\mathbf{x} = v_\alpha P_{st}(\mathbf{x},\mathbf{v}), \tag{12}$$

$$(I_\alpha^{rev})_\mathbf{v} = -\frac{1}{\tau\gamma}\left(\sum_\beta\left(\delta_{\alpha\beta}-\Omega\tau\varepsilon_{\alpha\beta}\right)\phi_\beta\right)P_{st}(\mathbf{x},\mathbf{v}), \tag{13}$$

$$(I_\alpha^{irr})_\mathbf{x} = 0, \tag{14}$$

$$(I_\alpha^{irr})_\mathbf{v} = -\frac{D_a}{\tau^2}\frac{\partial P_{st}(\mathbf{x},\mathbf{v})}{\partial v_\alpha} - \frac{1}{\tau}\sum_\beta\left(\delta_{\alpha\beta}+\frac{\tau}{\gamma}\phi_{\alpha\beta}-\Omega\tau\varepsilon_{\alpha\beta}\right)v_\beta P_{st}(\mathbf{x},\mathbf{v}). \tag{15}$$

Let us remark that the x-component (y-component) of the current depends on the y-component (x-component) of the gradient of the potential.

The system is microscopically reversible when the detailed balance condition holds.[35,36] Such a condition is satisfied if $\mathbf{I}_\alpha^{irr} = 0$ and $\mathbf{div}_\alpha\cdot\mathbf{I}_\alpha^{rev} = 0$ in the steady state.

2.2 Unconfined chiral active motion

In the free case $\phi = 0$, the time-independent solution of eqn (10) is the steady state distribution, P_{st}, and is uniform in space and has the form:

$$P_{\rm st}(\mathbf{x},\mathbf{v}) = \mathcal{N}\exp\left(-\frac{\tau}{2D_{\rm a}}\left(v_x^2+v_y^2\right)\right). \quad (16)$$

We notice that while the two-time properties of the velocity distribution depend on Ω, as already seen in eqn (5), the presence of chirality does not affect the shape of the Maxwell-like velocity distribution (16) with respect to the case $\Omega = 0$, a situation which is modified when the particles are confined as we show below.

We, now, consider how the torque Ω modifies the diffusive properties of the particles and find that for both the ABP and the AOUP the mean square displacement is given by the formula:[16,47]

$$\left\langle (x_\alpha(t)-x_\alpha(0))^2\right\rangle = 2\int_0^t {\rm d}t_1\int_0^{t_1}{\rm d}t_2\langle u_\alpha(t_1)u_\alpha(t_2)\rangle$$
$$= 2D_\Omega\left(t+\frac{(1-\Omega^2\tau^2)\tau}{1+\Omega^2\tau^2}\left(\mathrm{e}^{-t/\tau}\cos(\Omega t)-1\right)\right.$$
$$\left.-\frac{2\Omega\tau^2}{1+\Omega^2\tau^2}\mathrm{e}^{-t/\tau}\sin(\Omega t)\right), \quad (17)$$

where $D_\Omega = \dfrac{D_{\rm a}}{1+\Omega^2\tau^2}$ and the thermal contribution $2D_{\rm t}t$ to the mean square displacement has been neglected. One sees that the long-time diffusion coefficient is decreased by a factor $(1+\Omega^2\tau^2)^{-1}$ with respect to the non-chiral case,[37] an effect which is explained by noticing that the particles perform cycloid trajectories.

An easy check of the lack of detailed balance is provided by the free case whose distribution function is given by (16). At variance with the AOUP with $\phi = 0$, the condition that the components of the irreversible current must vanish is violated:

$$(I_x^{\rm irr})_{\mathbf{v}} = -\Omega v_y P_{\rm st}(\mathbf{v}) \neq 0, \quad (18)$$

$$(I_y^{\rm irr})_{\mathbf{v}} = \Omega v_x P_{\rm st}(\mathbf{v}) \neq 0. \quad (19)$$

3 Spontaneous circulation of totally confined active particles

We begin by considering a CAOUP moving in two dimensions and confined in a harmonic trap:[38]

$$\phi(\mathbf{x}) = k\frac{(x^2+y^2)}{2}.$$

The linearity of the Ornstein–Uhlenbeck process allows obtaining the exact form of the nonequilibrium steady state, whose phase-space distribution reads:

$$P(\mathbf{x},\mathbf{v}) = \mathcal{N}\exp\left[-\frac{\tau}{2D_{\rm a}}\Gamma\left(\left(v_x+\frac{\Gamma-1}{\Gamma}\Omega y\right)^2+\left(v_y-\frac{\Gamma-1}{\Gamma}\Omega x\right)^2\right)\right]$$
$$\times\exp\left[-\frac{1}{2D_{\rm a}\tau}\frac{\Gamma-1}{\Gamma}\left(\Gamma^2+\Omega^2\tau^2\right)\left(x^2+y^2\right)\right], \quad (20)$$

where $\Gamma = \left(1+\dfrac{\tau}{\gamma}k\right)$ with $k > 0$ and $\mathcal{N}$ is a normalization constant.

At variance with passive systems, the positional and velocity coordinates are correlated and the steady state is characterized by currents linearly increasing with $\Omega \neq 0$. In fact, the average velocity field at fixed position $\mathbf{x}$, defined as

$$\langle\mathbf{v}\rangle_{\mathbf{x}} = \frac{\int{\rm d}\mathbf{v}P(\mathbf{x},\mathbf{v})\mathbf{v}}{\int{\rm d}\mathbf{v}P(\mathbf{x},\mathbf{v})},$$

is given by the formulas:

$$\langle v_x\rangle_{\mathbf{x}} = -\frac{\Gamma-1}{\Gamma}\Omega y, \quad (21)$$

$$\langle v_y\rangle_{\mathbf{x}} = \frac{\Gamma-1}{\Gamma}\Omega x. \quad (22)$$

Such a field has the structure of a vortex centered at the minimum of the potential. The confining force pins to the origin of the trajectories of different particles resulting in producing a single coherent macroscopic vortex, which in contrast is absent in the free-case as evident from the distribution (16). Finally, the velocity variance

$$\langle v_x^2\rangle - \langle v_x\rangle^2 = \langle v_y^2\rangle - \langle v_y\rangle^2 = \frac{1}{\Gamma}\frac{D_{\rm a}}{\tau} \quad (23)$$

is reduced with respect to the free case being $\Gamma > 0$, but is torque independent.

We also consider the corresponding marginal (configurational) distribution, $\rho(x,y) = \int{\rm d}\mathbf{v}P(\mathbf{x},\mathbf{v})$:

$$\rho(x,y) = \mathcal{N}'\exp\left(-\frac{1}{2D_{\rm a}\tau}\frac{\Gamma-1}{\Gamma}\left(\Gamma^2+\Omega^2\tau^2\right)\left(x^2+y^2\right)\right). \quad (24)$$

We remark that the chirality determines a more concentrated distribution of the particles near the bottom of the potential well, thus effectively increasing its stiffness. In other words, the chirality acts as a centripetal force whose strength is proportional to $\Omega^2\tau^2$. The non-chiral limit $\Omega \to 0$ is smoothly recovered and one finds the well-known AOUP distribution in the quadratic trap.

By inserting the exact solution (20) in eqn (12)–(15) one finds that also in the case of harmonically confined chiral particles at variance with the non chiral AOUP the detailed balance condition is violated due to the presence of circulating currents. Due to this lack of detailed balance condition the unified colored noise approximation (UCNA)[39] fails even in this simple case of a chiral AOUP confined in a harmonic trap.[25]

3.1 Virial pressure

The virial pressure formula is obtained by equating the pressure exerted by the particles on the walls to force per unit length that the walls exert on the particles.[40,41] Thus, we obtain

$$2p_vA = \langle\nabla\phi\cdot\mathbf{x}\rangle, \quad (25)$$

where A is the area and the average is obtained using the steady state distribution. For the rotationally invariant harmonic trap we find using eqn (24) the following expression of the virial pressure

$$p_vA = \frac{D\gamma}{\Gamma+\dfrac{\Omega^2\tau^2}{\Gamma}}.$$

Such a result shows that the pressure decreases as Ω increases since the particles tend to be more localised near the bottom of the well with respect to the $\Omega = 0$ case.

4 Confinement in a channel

Before delving into the study of the confined chiral gas, let us briefly summarize some recent results concerning the case $\Omega = 0$: the self-propelled particles accumulate in the proximity of repulsive walls.[42,43] Such a phenomenon is more evident when the persistence time, τ, increases and D_a/τ is large with respect to the thermal noise amplitude, γD_t. In fact, a particle pushed by the self-propulsion force along the normal to the wall remains trapped there and escapes only when the propulsion direction changes, *i.e.* typically after a time τ. This mechanism leads to the formation of a peak in the proximity of each wall and is reflected in eqn (8) by the presence of a Stokes force term, $-\frac{1}{\tau}\Gamma(\mathbf{x})\cdot\mathbf{v}$, which opposes the motion and traps the particle near the walls. In the region where the potential gradients are negligible, instead, the particles undergo an underdamped motion and their density is almost uniform or smoothly varies in the presence of thermal noise ($D_t \neq 0$).[31]

Intuitively, we expect a reduction of the accumulation of the particles at the walls with chirality. In fact, the time, t_w, a particle spends in front of a wall is a decreasing function of $|\Omega|$, as we argue by considering the form of the two-time velocity autocorrelation function eqn (5), characterized by the two characteristic time-scales τ and $1/\Omega$. In the non-chiral limit, $\Omega = 0$, the residence time at the wall is $t_w \approx \tau$, because after this time a particle typically inverts its self-propulsion and goes back to the bulk. On the other hand, in the case $|\Omega| > 0$, the first value where the autocorrelation changes its sign is $t_\Omega = \pi/(2|\Omega|)$, the smallest zero of the cosine function in eqn (5). Based on this remark, we identify two regimes: (I) $t_\Omega \gg \tau$, where the role of the chirality is negligible and does not affect the distribution of the particles in the channel, hence $t_w \approx \tau$; (II) $t_\Omega \leq \tau$, where the correlation (5) changes the sign for times shorter than τ. In this case, we can estimate the typical time needed to change the orientation and leave the wall as $t_w \sim t_\Omega$. Following Lee,[44] we propose a coarse-grained description where the particles belong to two different populations: a bulk population of n_b members and a wall population of n_w elements, characterized by residence times t_b and t_w, respectively. Due to the permanent injection of energy, there is a continuous exchange of particles between the two populations, so that to achieve the steady state we must have $n_w/t_w = n_b/t_b$. We may conclude that the wall population decreases as t_w decreases, that is when Ω grows.

In the following, we employ two different types of set-ups in order to assess quantitatively the effects of chirality in confined systems. We begin with the study of an infinite parabolic channel where the particles are confined only in the x-direction and free to move along the y-direction. We shall determine the exact full steady state distribution function and show the existence of steady momentum currents induced by the chirality.

We then consider the more realistic slit case, *i.e.* a model where the wall and bulk regions are clearly separated and the walls are modeled by means of truncated repulsive harmonic potentials. In the case of non-constant potential curvature, it is possible to observe the interplay between wall accumulation and wall depletion due to the competition between wall attraction and a chiral effective force pushing the particles away from the boundaries.

4.1 Parabolic channel

A one dimensional quadratic well $\phi(\mathbf{x}) = k\frac{x^2}{2}$ mimics a channel limited by harmonic walls along the x-direction and unbounded along the y-direction. In this case, the distribution depends on the two components of the velocity $\mathbf{v}$, but only from the x-coordinate transversal to the channel. Its representation is a multivariate Gaussian distribution containing diagonal terms proportional to (v_x^2, v_y^2, x^2), but also three cross terms of type (v_xv_y, xv_y, xv_x). The exact expression of each of the six proportionality constants, featuring the Gaussian, is a function of the control parameters, k, τ, γ, Ω, D_a and is reported in Appendix B. In the main text, to ease the presentation we write the more transparent form of the distribution obtained by neglecting the contributions to the coefficients beyond the linear order in Ω:

$$P(\mathbf{x},\mathbf{v}) \approx N\exp\left[-\frac{\tau}{2D_a}\left(\Gamma v_x^2 + v_y^2 + 2\frac{\Gamma-1}{\Gamma}\Omega\tau v_x v_y\right)\right] \exp\left[-\frac{\Gamma-1}{2D_a\tau}\Gamma x^2\right]\exp\left[\Omega\frac{\tau}{D_a}\frac{\Gamma-1}{\Gamma}v_y x\right]. \tag{26}$$

By integrating over v_x and v_y we obtain the x-dependent average velocity along the y-direction as a function of Ω

$$\langle v_y\rangle_x = \frac{\Gamma-1}{\Gamma}\Omega x. \tag{27}$$

The result (27) is valid to all orders in Ω and for $\Omega > 0$ predicts the existence of a current parallel to the walls and directed along the downward y-direction for $x < 0$ and upwards for $x > 0$, while reversing the sign of Ω the current in the two halves of the channel changes the sign. Instead, there is no net average current $\langle v_x\rangle_x$ along the x-direction. Finally, using the exact form of the distribution given by eqn (46) we obtain the associated marginalized positional distribution function

$$\rho(x) = \mathcal{N}\exp\left(-\frac{1}{2D_a\tau}\frac{\Gamma-1}{\Gamma}\left(\Gamma^2+\Omega^2\tau^2\right)x^2\right) \tag{28}$$

which shows that the density near the center is enhanced with respect to the $\Omega = 0$ case as if an extra effective potential $\frac{\Gamma-1}{\Gamma}\Omega^2\tau^2x^2/2$ was pushing the particles towards the midpoint. In Fig. 1 we display two typical trajectories for two different values of Ω, which become more and more localised as the chirality increases.

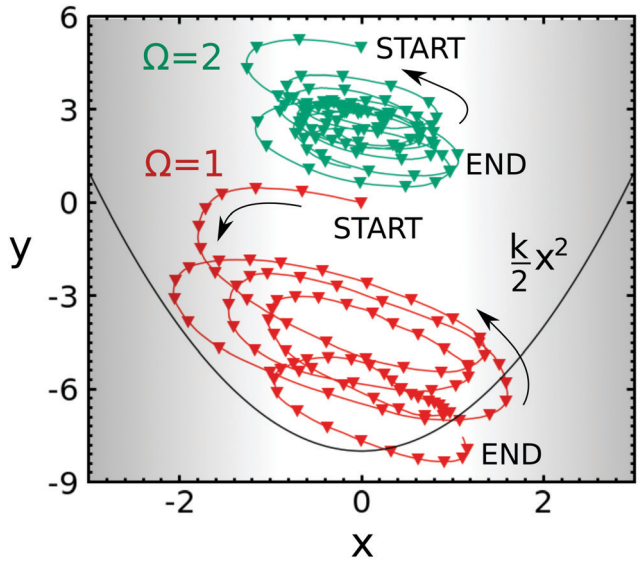

Fig. 1 Two typical trajectories of active chiral particles confined to a parabolic channel. The particles undergo spiral motion. Notice the stronger localisation of the particle near the bottom of the well, with increasing value of the torque Ω as predicted by eqn (28).

Unlike the rotationally invariant case, the variances of the velocity of the particles weakly depend on the value of Ω as shown by the exact solution of Appendix B:

$$\langle v_x^2 \rangle_{x=0} = \frac{D_a}{\tau} \frac{\Omega^2\tau^2 + \Gamma}{\Omega^2\tau^2 + \Gamma^2},$$

$$\langle v_y^2 \rangle_{x=0} = \frac{D_a}{\tau\Gamma} \frac{\Omega^2\tau^2 + \Gamma^3}{\Omega^2\tau^2 + \Gamma^2}$$

and

$$\langle v_x v_y \rangle_{x=0} = -\frac{D_a}{\tau}(\Gamma - 1)\frac{\Omega\tau}{\Omega^2\tau^2 + \Gamma^2}, \quad (29)$$

where the subscript means that the average refers to the midpoint $x = 0$.

4.2 The slit

We turn, now, to study a different type of channel where the stiffness of the walls and the width of the channel can be varied independently. A two-dimensional collection of independent chiral active particles is confined between two parallel repulsive soft walls, exerting a force piece-wise linear, characterized by an elastic constant k according to the formula:

$$F_w(x) = k(x + L)\Theta(-x - L) - k(x - L)\Theta(x - L), \quad (30)$$

where Θ is the Heaviside step-distribution. We choose a large value of k so that the penetration inside the wall is negligible. The space between the walls extending from $x = -L$ to $x = L$, instead, forms a force-free region. The setup, recently studied in the case of non-chiral particles, $\Omega = 0$, provides a more realistic description of a straight capillary because we may clearly distinguish a boundary, potential region from a bulk-like region.[31] In the numerical simulations, in order to model an infinite vertical channel we assume periodic boundary conditions along the y-direction. At variance with the non chiral case, where the problem becomes effectively one-dimensional, in the $\Omega \neq 0$ case, as already found in the previous Section 4.1, both x and y directions matter and the system develops a steady vertical momentum current and the bulk region becomes overpopulated with respect to the $\Omega = 0$ case.

In Fig. 2, we plot the density at the walls, n_w, as a function of Ω, for two different parameter configurations: we fix the ratio $D_a/\tau = 1$ and perform numerical simulations for $\tau = 1$ and $\tau = 10$. We evaluate n_w by counting the number of particles in the regions $x \leq -L$ and $x \geq L$, for the left and right wall, respectively. In the regime (I) identified in Section 4 the decrease of n_w is slower than that of $1/|\Omega|$, since the effect of the chirality does not affect the wall population being $t_\Omega > \tau$. On the other hand, in regime (II) the scaling $1/\Omega$ fairly agrees with the data for both choices of τ.

In Fig. 3 we show the marginalized distribution $\rho(x)$ for a system of active chiral particles subject to the dynamics of eqn (7) and (8) in the presence of the wall force (30). We consider the dependence of the profile on the internal torque by varying Ω and keeping D_a and τ fixed to values such that there is appreciable accumulation at the walls. Upon introducing a small chirality the accumulation at the walls is reduced, as shown in Fig. 3(a). In the intermediate regime of Ω, the role of the chirality is more consistent: on one hand, the particles accumulate in front of the wall (as in the case $\Omega = 0$), and on the other hand, the profile in the bulk is no longer flat-like. In particular, we observe an emptying phenomenon in a layer near the wall favoring the accumulation in the inner region, as shown in Fig. 3(b). A further increase of Ω depletes the density near the walls and enhances it in the bulk region until the wall region remains almost completely empty. For these values of Ω, the situation is completely inverted with respect to the case $\Omega = 0$ and the wall behaves as if the effective wall-potential was repulsive.

We stress that, at variance with the harmonically confined CAOUP of Section 4.1, it is possible to observe a transition from

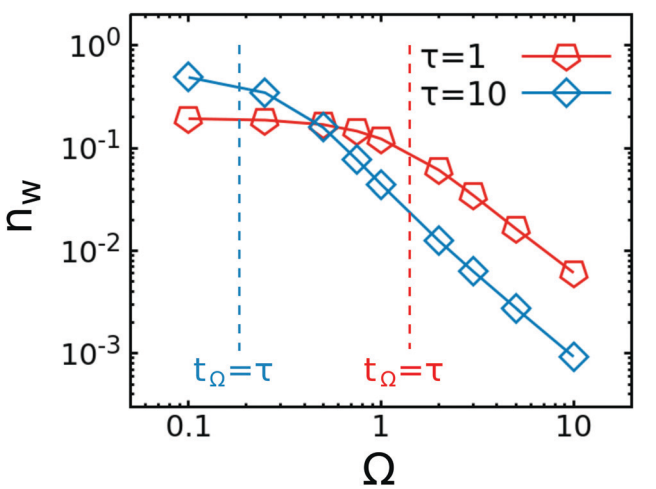

Fig. 2 Density at the walls n_w *versus* Ω for two different values of $\tau = 1$ (red pentagons) and 10 (blue diamonds). The parameters are: $D_a = \tau$, $\gamma = 1$, $k = 10$, and $L = 8$, and the walls are at positions $x = \pm L$.

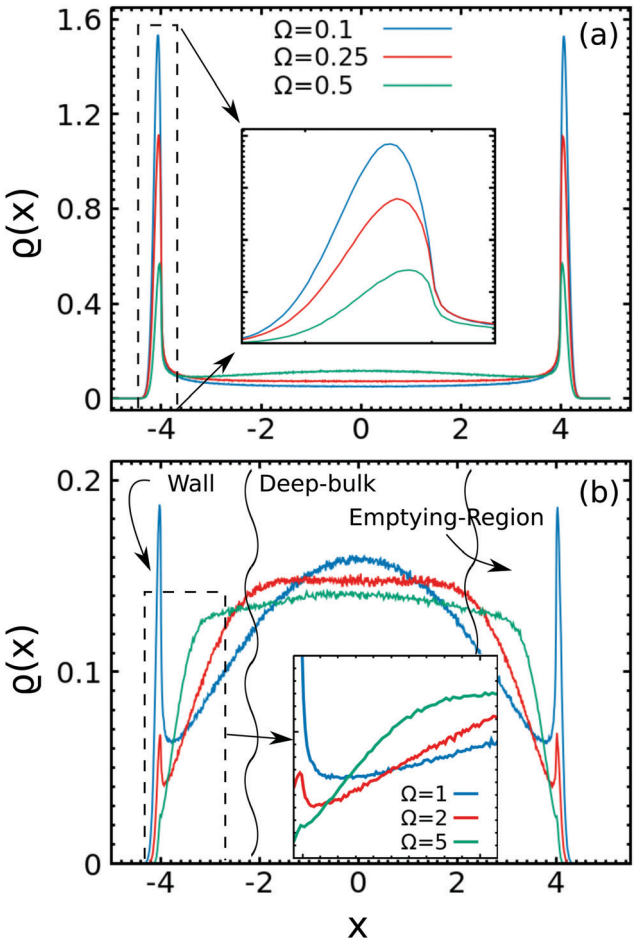

Fig. 3 Density profile $\rho(x)$ for different values of Ω as shown in the legend: Ω = 0.1, 0.25, 0.5 (panel (a)), Ω = 1, 2, 5 (panel (b)). The control parameters are: D_a = 10, τ = 10, γ = 1, k = 10 and L = 4. In the insets, we show the zoomed profiles of regions delimited by dashed vertical lines.

a situation where particles accumulate near the walls to a situation where they accumulate in the bulk.

We, now, explain the process which leads to the emptying of the wall region and to the enrichment of the central region in the case of the channel when $\Omega \neq 0$ and to this purpose we rewrite eqn (8) under the explicit form:

$$\dot{v}_x = -[1+(\Gamma-1)(\Theta(-x-L)+\Theta(x-L))]\frac{v_x}{\tau} - \Omega v_y - \Theta(-x-L)\frac{k}{\gamma\tau}(x+L) - \Theta(x-L)\frac{k}{\gamma\tau}(x-L) + \frac{\sqrt{2D_a}}{\tau}\eta_x$$

$$\dot{v}_y = -\frac{v_y}{\tau} + \Omega v_x + \frac{\Omega}{\gamma\tau}[k(x+L)\Theta(-x-L) + k(x-L)\Theta(x-L)] + \frac{\sqrt{2D_a}}{\tau}\eta_y.$$

One sees that on one side the chirality acts as an effective magnetic field of strength Ω periodically rotating the velocity direction without changing its magnitude and the other side, for $|x| > L$, in combination with the wall repulsion it produces a tangential force always along the y direction. As a result, the particle accelerates and gains "kinetic energy". Such a force, proportional to $k\Omega/\tau$ only acts in the boundary region and generates a vertical momentum current having opposite directions at the two walls. When a particle penetrates the potential region, its velocity components v_x is strongly damped by the large Stokes force $-\Gamma v_x/\tau$ and thus it remains trapped there. At the same time, the v_y component of the velocity rapidly increases under the action of the tangential force. This process continues for a time t_Ω after which the torque rotates the velocity vector and transfers the accumulated "kinetic energy" to the x component of the velocity pointing towards the bulk. In the regime of large $|\Omega|\tau \gg 1$, the tangential field acts on a shorter time scale than the scale of the dissipative Stokes force and the velocity is nearly unaffected by friction. The particle leaves the wall with a velocity proportional to Ω and enters the potential-free region where it undergoes a spiral motion with a large initial radius, due to the energy accumulated at the wall. This radius continuously shrinks due to the dissipation caused by the Stokes bulk force, as shown in Fig. 4. After a time $\sim\tau$ the dissipation becomes relevant and $\langle|v|\rangle \sim \sqrt{D_a/\tau}$, *i.e.* the steady state typical velocity. The process herein described continues forever since a fluctuation of the self-propulsion can drive a bulk particle to reach again the wall region to start a new cycle. It is clear that the removal of particles from the walls due to Ω has an effect on depleting the wall accumulation and increasing the bulk population.

To test the existence of large surface currents leading to the formation of an intermediate emptying region we have studied the profile of the vertical velocity. In the two panels Fig. 5 shows the average velocity $\langle v_y\rangle_x$ as a function of distance from the center of the slit x for two different values of Ω. We notice the monotonic behavior of the velocity, which can be described by a hyperbolic sine function since the average velocity in the

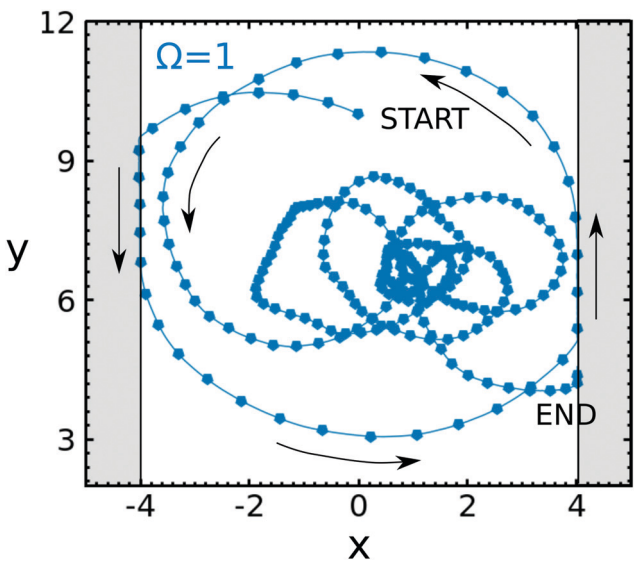

Fig. 4 A typical trajectory of an active chiral particle confined to a slit-like channel. In the inner region, the particle undergoes spiral-like motion, while at the walls it slides vertically. Notice that the sliding occurs downwards at the left wall and upwards at the right wall.

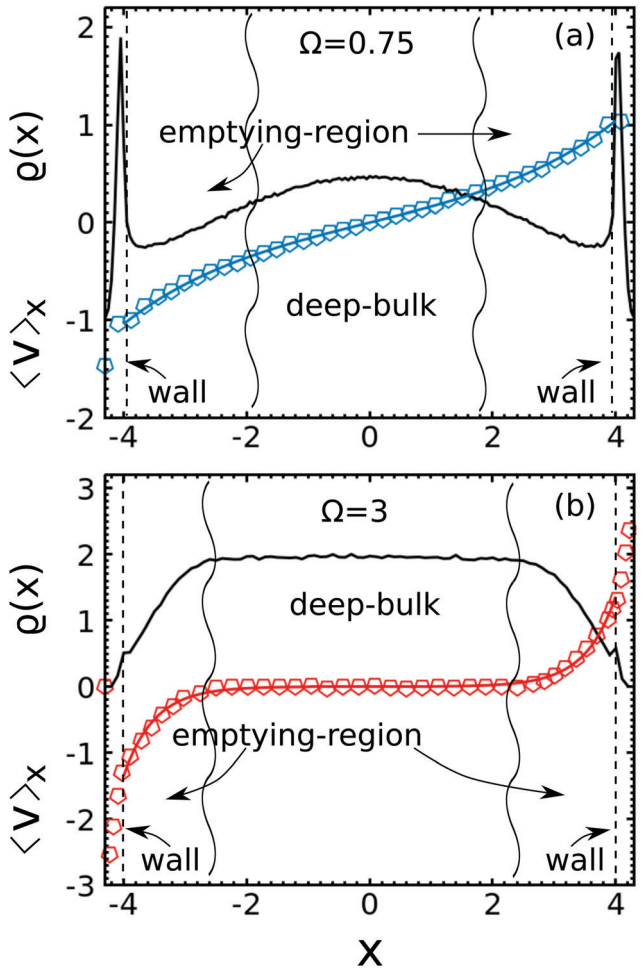

Fig. 5 Velocity and density profiles of the slit-like channel. Panel (a): case $\Omega = 0.75$. Mean vertical velocity $\langle v_y \rangle_x$ as a function of the x-coordinate (blue symbols) and theoretical prediction (blue line) eqn (41). The black line indicates the corresponding density profile $\rho(x)$. Panel (b): case $\Omega = 3$. Mean vertical velocity $\langle v_y \rangle_x$ *versus* x (red symbols) and theoretical prediction (red line) eqn (41). The black line indicates the density profile $\rho(x)$. For both panels the control parameters are: $\tau = 10$, $\gamma = 1$, $D_a = 10$, and $L = 4$.

left-hand side has the opposite direction with respect to the velocity in the right-hand side. As discussed above, the mechanism which causes such a behavior is the interplay between the wall force and the chiral force; however, in this case, the non-uniformity of the Stokes force in the x-direction leads to a richer structure both in the density and in the velocity profiles than the one observed in the parabolic channel. In fact, the Stokes force opposing the motion along the x direction is large only in the wall region $|x| > L$, while the centripetal force $\Omega\hat{\mathbf{z}} \times \mathbf{v}$ is spatially uniform.

4.3 Momentum profile in the potential-free region $|x| < L$ and effective viscosity

As shown in the two panels of Fig. 5, the vertical component of the average velocity field varies in the region bounded by the walls. Hereafter, we derive the equations for the current by projecting the Fokker-Planck equation onto an appropriate hydrodynamic space.

By integrating the FPE (10) over v_x,v_y we obtain the continuity equation:

$$\frac{\partial \rho(\mathbf{x},t)}{\partial t} + \frac{\partial j_x(\mathbf{x},t)}{\partial x} + \frac{\partial j_y(\mathbf{x},t)}{\partial y} = 0 \tag{31}$$

with

$$j_\alpha(\mathbf{x},t) = \int \mathrm{d}v_x \mathrm{d}v_y v_\alpha P(\mathbf{x},\mathbf{v},t).$$

In the steady state $\frac{\partial j_x(x,t)}{\partial x} = 0$ and by symmetry the particle current $\mathbf{j}$ is a function of x only. From the continuity equation and the wall boundary conditions it follows that $j_x(x) = 0$, while the vertical component $j_y(x)$ varies with x. Next, we define the pressure tensor $\mathscr{P}$ as:

$$\mathscr{P}_{\alpha\beta}(\mathbf{x}) = \int \mathrm{d}v_x \mathrm{d}v_y v_\alpha v_\beta P(\mathbf{x},\mathbf{v}),$$

the stationary FPE is multiplied by v_y and v_x, respectively, and integrated over the velocity. In the potential-free region, $|x| < L$, we obtain the following equations relating the components of the pressure tensor to the current j_y:

$$-\frac{1}{\tau} j_y(x) - \frac{\partial \mathscr{P}_{xy}(x)}{\partial x} = 0, \tag{32}$$

$$-\Omega j_y(x) - \frac{\partial \mathscr{P}_{xx}(x)}{\partial x} = 0. \tag{33}$$

In order to determine $j_y(x)$ from eqn (32), we must relate it to $\mathscr{P}_{xy}(x)$, a task which will be pursued hereafter using a simple kinetic argument.

In the situation depicted in Fig. 5, let us consider the average vertical momentum flux J_y^+ per unit time and per unit length crossing a segment at $x = x_0$ (with $-L < x_0 < L$) and originating from the region $x < x_0$. We assume that: (a) the particles passing from the one side to the other side of the unit vertical segment at x_0 move with the constant average velocity, $|\bar{v}_x|$ and (b) the physical space can be divided into cells of linear size λ_Ω, the smallest distance over which the mean values of the physical observables vary. Based on these hypotheses, the magnitude of J_y^+ can be written as:

$$J_y^+(x_0) = \frac{1}{4}|\bar{v}_x| j_y(x_0 - \lambda_\Omega). \tag{34}$$

Similarly, the momentum flux of the particles coming from the right is

$$J_y^-(x_0) = -\frac{1}{4}|\bar{v}_x| j_y(x_0 + \lambda_\Omega), \tag{35}$$

where the geometrical factor 1/4 takes into account the different possible directions of the velocities of the particles under the assumption of isotropy of the velocity distribution. The result is a net transfer of the y-component of momentum across the segment $x = x_0$ given by:

$$J_y^+(x_0) - J_y^-(x_0) \approx -\frac{1}{2}\lambda_\Omega |\bar{v}_x| \left.\frac{\partial j_y}{\partial x}\right|_{x_0}. \tag{36}$$

The rate of change of momentum per unit length, $(J_y^+ - J_y^-)$, due to the diffusion of the particles in the horizontal direction is equivalent to the shear force per unit length exerted by the particles with $x < x_0$ on the particles with $x > x_0$, that is to the off-diagonal component of the pressure tensor:

$$\mathscr{P}_{xy} = J_y^+ - J_y^- = -\nu_\Omega \frac{\partial j_y}{\partial x} \tag{37}$$

with $\nu_\Omega = \frac{1}{2}\lambda_\Omega |\bar{v}_x|$. The same kind of elementary kinetic argument, this time replacing the transported quantity $j_y(x)$ by $\rho(x)$, predicts that a gas of tracer chiral active particles with non uniform density $\rho(x)$ generates a net flux J_N, defined as the number of particles per unit time crossing a unit vertical segment according to the formula:

$$J_N = -\frac{1}{2}\lambda_\Omega |\bar{v}_x| \left.\frac{\partial \rho(x)}{\partial x}\right|_{x_0}. \tag{38}$$

The ratio between $-J_N$ and $-\frac{\partial \rho(x)}{\partial x}$ defines the self-diffusion coefficient of chiral particles $D_\Omega = \frac{1}{2}\lambda_\Omega |\bar{v}_x|$. One concludes that the kinematic shear viscosity and the diffusion coefficient are equal: $\nu_\Omega = D_\Omega$, a result well known in the kinetic theory of dilute gases. By comparing this result with the exact calculation of the long-time diffusion coefficient $D_\Omega = \frac{D_a}{1+\Omega^2\tau^2}$ given by eqn (17) we can now directly determine the value of ν_Ω and thus obtain

$$\mathscr{P}_{xy} = -\frac{D_a}{1+\Omega^2\tau^2}\frac{\partial j_y}{\partial x}. \tag{39}$$

Finally, substituting in eqn (32) we obtain

$$\frac{\partial^2 j_y}{\partial x^2} = \frac{1+\Omega^2\tau^2}{D_a \tau} j_y \tag{40}$$

whose solution is

$$j_y(x) = A \sinh\left(\frac{x}{\sqrt{\nu_\Omega \tau}}\right) = A \sinh\left(\frac{\sqrt{1+\Omega^2\tau^2}}{\sqrt{D_a \tau}} x\right), \tag{41}$$

where the constant A is fixed by the odd boundary conditions at $x = \pm L$. Using eqn (33) we can obtain $\mathscr{P}_{xx}$:

$$\mathscr{P}_{xx}(x) = \int_{-L}^{x} \mathrm{d}x' j_y(x') = \mathscr{P}_0 - A\Omega\sqrt{\nu_\Omega \tau}\cosh\left(\frac{x}{\sqrt{\nu_\Omega \tau}}\right), \tag{42}$$

where the constant $\mathscr{P}_0$ is determined by the boundary conditions. Let us remark that $j_y(x)$ is proportional to $\langle v_y \rangle_x$ in the regime where the density $\rho(x)$ varies slower than $\langle v_y \rangle_x$ itself. Under these conditions it is legitimate to compare directly the solution $j_y(x)$ of eqn (41) with the profile $\langle v_y \rangle_x$ of Fig. 5. The present prediction of the current profile $j_y(x)$ (eqn (41)) is in qualitative agreement with the numerical simulation result for the same quantity. However, in order to achieve a full quantitative agreement it is necessary to multiply the theoretical characteristic length $l = \sqrt{\nu_\Omega \tau}$ by a factor $\sqrt{2}$. The origin of such a rescaling cannot be explained by our simple argument and remains to be understood.

5 Conclusions

In this paper, we have introduced an extension of the active Ornstein–Uhlenbeck model to study the behavior of a gas of active chiral particles under confinement. The handedness of the particles' motion has been accounted for by means of an effective torque term in the self-propulsion forcing. The presence of the torque has a profound influence on the properties of the AOUP as it breaks the detailed balance condition even in the unconfined case. Under confinement, we find that the torque is responsible for the appearance of steady momentum currents and reduction of the accumulation of the particles at the container's boundaries. Explicit illustrations of these phenomena are shown by means of the exact solution of the stationary Fokker–Planck equation in two cases of parabolic confinement. In a more realistic case of confinement by stiff walls, beside the emptying of the boundary region and the enrichment of the bulk region, we find a structure of the velocity field akin to the one observed in sheared viscous fluids. This behavior is explained in terms of a simple kinetic argument and the velocity profile is reproduced.

Since the linear propulsive and rotational behavior can independently be tuned, by changing τ and Ω respectively, one could drive more efficiently the motion of active particles for instance by partly suppressing their diffusivity, or obtain more efficient harmonic traps. Active rotation does also have an impact on the properties of interacting systems: Liao and Klapp have found that it generally opposes motility-induced clustering and phase separation, as demonstrated by narrowing the coexistence region of a two-dimensional chiral ABP upon increase of the propulsion angular velocity.[45] A similar behaviour should also be observed in systems of the interacting CAOUP.

Finally, concerning the practical interest of the systems studied, one could envisage the possibility of selecting chiral active particles on the basis of their handedness in pharmaceutical or biotechnological applications where chiral levogyre or dextrogyre properties correspond to different functionalities.[20,46]

Conflicts of interest

There are no conflicts of interest to declare.

Appendix A: transformation of variables

In this appendix, we derive the governing equations for the transformed variables (x_i, v_i). Let us consider the AOUP equation:

$$\dot{x}_i = -\frac{1}{\gamma}\frac{\partial \phi}{\partial x_i} + \sqrt{2D_t}\xi_i + u_i \tag{43}$$

and define the "velocity", v_i: $v_i = \dot{x}_i - \sqrt{2D_t}\xi_i(t)$. We differentiate (43) and eliminate u_i with the help of eqn (4) and use again (43). Adopting Stratonovich convention for the derivatives of ϕ we finally obtain:

$$\dot{x}_i = v_i + \sqrt{2D_t}\xi_i \tag{44}$$

$$\dot{v}_i = -\frac{1}{\tau}\left[\frac{1}{\gamma}\frac{\partial\phi}{\partial x_i}+v_i\right]+\Omega\varepsilon_{ik}\left[v_k+\frac{1}{\gamma}\frac{\partial\phi}{\partial x_k}\right]-\frac{1}{\gamma}\frac{\partial^2\phi}{\partial x_i\partial x_k}v_k + \frac{\sqrt{2D_a}}{\tau}\eta_i-\frac{\sqrt{2D_t}}{\gamma}\frac{\partial^2\phi}{\partial x_i\partial x_k}\xi_k \quad (45)$$

where we used the Einstein repeated index convention.

Appendix B: exact distribution in the parabolic channel

Hereafter, we report the exact phase-space distribution in the case of a parabolic channel. Its form as discussed in the main text depends on six constants A, K_1, K_2, K_3, M_1, and N_2 according to the formula:

$$P(\mathbf{x},\mathbf{v}) = \mathcal{N}\exp\left(-\frac{A}{2}x^2\right)\exp\left(-\frac{K_1}{2}v_x{}^2-\frac{K_2}{2}v_y{}^2-K_3v_xv_y\right) \times\exp\left(-M_1v_xx-N_2v_yx\right). \quad (46)$$

For the sake of notational simplicity we define:

$$\Delta = \Omega^2\tau^2+\Gamma^2$$

and write the following six equations for the coefficients in terms of independent control parameters:

$$A = \frac{k}{D_a\gamma}\frac{\Omega^4\tau^4+2\Omega^2\tau^2+3\Omega^2\tau^2(\Gamma-1)+\Gamma^3}{\Delta},$$

$$K_1 = \frac{\tau}{D_a}\frac{\Omega^2\tau^2+\Gamma^3}{\Delta},$$

$$K_2 = \frac{\tau}{D_a}\Gamma\frac{\Omega^2\tau^2+\Gamma}{\Delta},$$

$$K_3 = \frac{\Omega\tau^3}{D_a\gamma}\frac{\Gamma}{\Delta}k,$$

$$M_1 = -\Omega^2\tau^4\frac{1}{D_a\gamma}\frac{k^2}{\gamma}\frac{1}{\Delta},$$

$$N_2 = -\frac{\Omega\tau^2}{D_a\gamma}\frac{\Omega^2\tau^2+\Gamma}{\Delta}k.$$

The average velocity along y is

$$\langle v_y\rangle_x = \frac{\Gamma-1}{\Gamma}\Omega x \quad (47)$$

and is proportional to $\frac{\Omega\tau}{\gamma}k$.

Acknowledgements

We thank Andrea Puglisi and Claudio Maggi for illuminating discussions.

References

1 S. Ramaswamy, *Annu. Rev. Condens. Matter Phys.*, 2010, **1**, 323–345.
2 C. Bechinger, R. Di Leonardo, H. Löwen, C. Reichhardt, G. Volpe and G. Volpe, *Rev. Mod. Phys.*, 2016, **88**, 045006.
3 M. Marchetti, J. Joanny, S. Ramaswamy, T. Liverpool, J. Prost, M. Rao and R. A. Simha, *Rev. Mod. Phys.*, 2013, **85**, 1143.
4 P. Romanczuk, M. Bär, W. Ebeling, B. Lindner and L. Schimansky-Geier, *Eur. Phys. J.: Spec. Top.*, 2012, **202**, 1–162.
5 H. C. Berg and L. Turner, *Biophys. J.*, 1993, **65**, 2201–2216.
6 E. Lauga, W. R. DiLuzio, G. M. Whitesides and H. A. Stone, *Biophys. J.*, 2006, **90**, 400–412.
7 B. Friedrich and F. Jülicher, *New J. Phys.*, 2008, **10**, 123025.
8 W. R. DiLuzio, L. Turner, M. Mayer, P. Garstecki, D. B. Weibel, H. C. Berg and G. M. Whitesides, *Nature*, 2005, **435**, 1271.
9 M. Loose and T. J. Mitchison, *Nat. Cell Biol.*, 2014, **16**, 38.
10 F. Kümmel, B. ten Hagen, R. Wittkowski, I. Buttinoni, R. Eichhorn, G. Volpe, H. Löwen and C. Bechinger, *Phys. Rev. Lett.*, 2013, **110**, 198302.
11 H. Löwen, *Eur. Phys. J.: Spec. Top.*, 2016, **225**, 2319–2331.
12 R. Blakemore, *Science*, 1975, **190**, 377–379.
13 C. T. Lefèvre and D. A. Bazylinski, *Microbiol. Mol. Biol. Rev.*, 2013, **77**, 497–526.
14 B. Ten Hagen, R. Wittkowski, D. Takagi, F. Kümmel, C. Bechinger and H. Löwen, *J. Phys.: Condens. Matter*, 2015, **27**, 194110.
15 A. Najafi and R. Golestanian, *Phys. Rev. E: Stat., Nonlinear, Soft Matter Phys.*, 2004, **69**, 062901.
16 S. van Teeffelen and H. Löwen, *Phys. Rev. E: Stat., Nonlinear, Soft Matter Phys.*, 2008, **78**, 020101.
17 W. Ebeling, F. Schweitzer and B. Tilch, *BioSystems*, 1999, **49**, 17–29.
18 M. Cates and J. Tailleur, *EPL*, 2013, **101**, 20010.
19 G. Szamel, *Phys. Rev. E: Stat., Nonlinear, Soft Matter Phys.*, 2014, **90**, 012111.
20 M. Mijalkov and G. Volpe, *Soft Matter*, 2013, **9**, 6376–6381.
21 G. Volpe, S. Gigan and G. Volpe, *Am. J. Phys.*, 2014, **82**, 659–664.
22 Y. Li, P. K. Ghosh, F. Marchesoni and B. Li, *Phys. Rev. E: Stat., Nonlinear, Soft Matter Phys.*, 2014, **90**, 062301.
23 B.-q. Ai, Y.-f. He and W.-r. Zhong, *Soft Matter*, 2015, **11**, 3852–3859.
24 X. Ao, P. K. Ghosh, Y. Li, G. Schmid, P. Hänggi and F. Marchesoni, *EPL*, 2015, **109**, 10003.
25 U. M. B. Marconi and C. Maggi, *Soft Matter*, 2015, **11**, 8768–8781.
26 S. Das, G. Gompper and R. G. Winkler, *New J. Phys.*, 2018, **20**, 015001.
27 L. Caprini, U. M. B. Marconi and A. Puglisi, *Sci. Rep.*, 2019, **9**, 1386.
28 Y. Fily and M. C. Marchetti, *Phys. Rev. Lett.*, 2012, **108**, 235702.
29 T. F. Farage, P. Krinninger and J. M. Brader, *Phys. Rev. E: Stat., Nonlinear, Soft Matter Phys.*, 2015, **91**, 042310.
30 U. M. B. Marconi, N. Gnan, M. Paoluzzi, C. Maggi and R. Di Leonardo, *Sci. Rep.*, 2016, **6**, 23297.

31 L. Caprini and U. M. B. Marconi, *Soft Matter*, 2018, **14**, 9044–9054.
32 J. R. Howse, R. A. Jones, A. J. Ryan, T. Gough, R. Vafabakhsh and R. Golestanian, *Phys. Rev. Lett.*, 2007, **99**, 048102.
33 H. Risken, *Fokker–Planck Equation*, Springer, 1984.
34 A. Puglisi and U. Marini Bettolo Marconi, *Entropy*, 2017, **19**, 356.
35 M. Cates, *Rep. Prog. Phys.*, 2012, **75**, 042601.
36 U. M. B. Marconi, A. Puglisi and C. Maggi, *Sci. Rep.*, 2017, **7**, 46496.
37 B. ten Hagen, S. van Teeffelen and H. Löwen, *J. Phys.: Condens. Matter*, 2011, **23**, 194119.
38 O. Dauchot and V. Démery, *Phys. Rev. Lett.*, 2019, **122**, 068002.
39 P. Hanggi and P. Jung, *Adv. Chem. Phys.*, 1995, **89**, 239–326.
40 U. M. B. Marconi, C. Maggi and S. Melchionna, *Soft Matter*, 2016, **12**, 5727–5738.
41 U. Marini Bettolo Marconi, C. Maggi and M. Paoluzzi, *J. Chem. Phys.*, 2017, **147**, 024903.
42 H. Wensink and H. Löwen, *Phys. Rev. E: Stat., Nonlinear, Soft Matter Phys.*, 2008, **78**, 031409.
43 J. Elgeti and G. Gompper, *EPL*, 2013, **101**, 48003.
44 C. F. Lee, *New J. Phys.*, 2013, **15**, 055007.
45 G.-J. Liao and S. H. Klapp, *Soft Matter*, 2018, **14**, 7873–7882.
46 S. Meinhardt, J. Smiatek, R. Eichhorn and F. Schmid, *Phys. Rev. Lett.*, 2012, **108**, 214504.
47 F. J. Sevilla, *Phys. Rev. E*, 2016, **94**, 062120.